Journal of Alloys and Compounds 752 (2018) 68–75

Contents lists available at ScienceDirect

Journal of Alloys and Compounds

journal homepage: http://www.elsevier.com/locate/jalcom

Self-organized TiO_2 network decorated with SnO_2 nanoparticles as an anode for lithium-ion batteries

Xue Li [a], Ziyi Zhu [a], Girish Praveen Nayaka [a], Jianguo Duan [a], Ding Wang [a], Peng Dong [a], Ling Huang [b], Jinbao Zhao [b], Shigang Sun [b], Xiaohua Yu [c, *], Yingjie Zhang [a, **]

[a] National and Local Joint Engineering Laboratory for Lithium-ion Batteries and Materials Preparation Technology, Key Laboratory of Advanced Battery Materials of Yunnan Province, Faculty of Metallurgical and Energy Engineering, Kunming University of Science and Technology, Kunming, 650093, China
[b] State Key Laboratory of Physical Chemistry of Solid Surfaces, Collaborative Innovation Center of Chemistry for Energy Materials, College of Chemistry and Chemical Engineering, Xiamen University, Xiamen, 361005, China
[c] National Engineering Research Center of Waste Resource Recovery, Kunming University of Science and Technology, Kunming, 650093, China

ARTICLE INFO

Article history:
Received 17 October 2017
Received in revised form
12 April 2018
Accepted 13 April 2018
Available online 14 April 2018

Keywords:
Ti-based materials
Tin oxide
Lithium-ion batteries
Flexible electrodes
Binder free

ABSTRACT

An efficient synthesis method is developed by combining hydrothermal and pyrolysis methods to fabricate the TiO_2@SnO_2 film electrode with a special three-dimensional (3D) nano-network structure. In the present study, the TiO_2 network can offer a 3D scaffold for the SnO_2 nanoparticles against the drastic pulverization problem and also support a fast charge transport path. When being assessed as an anode for lithium-ion batteries (LIBs), the unique structure eventually brings relatively stable cycling processes (834 mAh g^{-1} can be maintained after 100 cycles with high capacity retention of 120%) and a remarkable rate performance (796, 705, 564 and 464 mAh g^{-1} at 200, 400, 800 and 1600 mA g^{-1}, respectively).

1. Introduction

LIBs are regarded as one of the best sources of energy with a high conversion efficiency of chemical energy to electric energy without any pollution. Among the different types of commercial anode materials for LIBs, tin dioxide materials are considered as promising anode materials owing to their relative abundance, low cost, compatibility, and high theoretical capacity (782 mAh g^{-1}), which is more than twice that of graphite (370 mAh g^{-1}) [1]. Furthermore, tin dioxide offers a relatively high lithiation potential, which can control the electroplating of lithium leading to high safety of the materials.

Nevertheless, while SnO_2 shows good specific capacity, it suffers from large volume expansion (300%) [2] and the formation of a solid electrolyte interface (SEI) film on the surface of electrode [3,4], which leads to rapid deterioration and pulverization during cycling. Furthermore, the low conductivity of SnO_2 affects the electrochemical performance, especially at high current densities. Many research studies have been carried out to solve those problems through a unique morphological design for pure SnO_2 anodes. Unfortunately, there is little advancement for pure SnO_2 anodes with these designs.

Developing hybrid nanostructures has been regarded as another effective method. Among the hybrid nanostructures, TiO_2 hybrid nanocomposites are encouraging electrode materials for LIBs due to their integral safety and excellent electrochemical performance. Among the hybrid nanostructures, TiO_2 hybrid nanocomposites, including nanotubes, nanowires, double-shelled nano-spheres and hollow micro-tubes etc., are encouraging electrode materials for LIBs due to the inherent safety and excellent electrochemical performance [5–8].

Table 1 summarizes the electrochemical performance of SnO_2-based materials from the various literature sources. Interestingly, similar morphologies can result in radically different electrochemical performances [9–29]. By comparison, pure SnO_2 with a unique nanostructure usually shows a relatively unstable cycling performance [9,10]. In order to resolve this problem, many researchers have simultaneously introduced graphene and TiO_2 to

* Corresponding author.
** Corresponding author.
E-mail address: 438616074@qq.com (X. Yu).

https://doi.org/10.1016/j.jallcom.2018.04.161
0925-8388/

Table 1
Recently reported LIBs systems based on SnO_2 and SnO_2 hybrid electrodes.

Materials	Rate performance	Cycling performance	Ref.
Mesoporous hollow SnO_2 nanococoons	360 mAh g^{-1} for 5 C	666 mAh g^{-1} for 0.3 C	[9]
Mesoporous SnO_2 microspheres	200 mAh g^{-1} for 2 A g^{-1}	370 mAh g^{-1} for 1 A g^{-1}	[10]
Graphene–TiO_2–SnO_2	250 mAh g^{-1} for 1000 mA g^{-1}	537 mAh g^{-1} for 50 mA g^{-1}	[11]
TiO_2–SnO_2 @graphene	388 mAh g^{-1} for 1.5 A g^{-1}	617 mAh g^{-1} for 0.4 A g^{-1}	[12]
TiO_2-SnO_2-graphene aerogels	470 mAh g^{-1} for 1 A g^{-1}	750 mAh g^{-1} for 0.1 A g^{-1}	[13]
SnO_2@TiO_2	200 mAh g^{-1} for 2000 mA g^{-1}	445 mAh g^{-1} for 800 mA g^{-1}	[14]
SnO_2–TiO_2@ graphene	611 mAh g^{-1} for 2000 mA g^{-1}	1276 mAh g^{-1} for 200 mA g^{-1}	[15]
Graphene-based TiO_2/SnO_2 hybrid nanosheets	260 mAh g^{-1} for 4000 mA g^{-1}	600 mAh g^{-1} for 160 mA g^{-1}	[16]
Graphene/SnO_2 nanorod/carbon nanostructures	540 mAh g^{-1} for 3 C	983 mAh g^{-1} for 0.1 C	[17]
SnO_2 encapsulated TiO_2 hollow nanofibers	244 mAh g^{-1} for 10 C	517 mAh g^{-1} for 0.2 C	[18]
Graphene nanoribbon and nanostructured SnO_2	580 mAh g^{-1} for 2 A g^{-1}	825 mAh g^{-1} for 100 mA g^{-1}	[19]
Carbon encapsulated SnO_2@ graphene/TiO_2 nanocomposites	476 mAh g^{-1} for 1000 mA g^{-1}	1131 mAh g^{-1} for 100 mA g^{-1}	[20]
SnO_2@TiO_2 nanospheres	536 mAh g^{-1} for 1000 mA g^{-1}	838.1 mAh g^{-1} for 200 mA g^{-1}	[21]
N-doped a-TiO_2 nanotube	100 mAh g^{-1} for 10 C	200 mAh g^{-1} for 0.1 C	[22]
hierarchical TiO_2/SnO_2 hollow	440 mAh g^{-1} for 1000 mA g^{-1}	644.7 mAh g^{-1} for 100 mA g^{-1}	[23]
spheres coated with graphitized carbon	218 mAh g^{-1} for 5000 mA g^{-1}		
Ternary SnO_2-Co-C composite	610 mAh g^{-1} for 2000 mA g^{-1} after 1000 cycles	780 mAh g^{-1} for 200 mA g^{-1} after 400 cycles	[24]
Graphene/SnO_2/polyacrylamide nanocomposites	376 mAh g^{-1} for 5 A g^{-1} after 300 cycles	989 mAh g^{-1} for 0.2 A g^{-1}	[25]
Carbon-riveted graphene/SnO_2	445 mAh g^{-1} for 1000 mA g^{-1} after 250 cycles	815 mAh g^{-1} for 100 mA g^{-1} after 150 cycles	[26]
Hierarchical hollow SnO_2 microspheres	463 mAh g^{-1} for 5 C	659 mAh g^{-1} for 0.1 C after 50 cycles	[27]
PAN-based carbon fiber@SnO_2	225 mAh g^{-1} for 2000 mA g^{-1}	433 mAh g^{-1} for 100 mA g^{-1}	[28]
Bamboo carbon fiber@SnO_2@carbon composites	409.1 mAh g^{-1} for 1000 mA g^{-1}	627.1 mAh g^{-1} for 100 mA g^{-1} after 100 cycles	[29]
3D nano-network TiO_2@SnO_2	464 mAh g^{-1} for 1600 mA g^{-1}	836 mAh g^{-1} for 200 mA g^{-1}	Our work

improve the electrochemical performance [11–17]. However, the related preparation processes are very complicated and costly. In our work, 3D network TiO_2 was simply prepared via a facile hydrothermal method, which can be used as stable barriers via facile to effectively prevent SnO_2 from agglomeration. The superior electrochemical performance of the prepared TiO_2@SnO_2 anode was better than that of the most recently reported works on SnO_2 nanostructures and SnO_2 hybrid composite anodes.

In the present work, we use a self-organized TiO_2 network to tightly hold SnO_2 nanoparticles. The TiO_2 network can offer a 3D scaffold for the SnO_2 nanoparticles and a charge transport path. Here, the porous structure was expected to provide short pathways for lithium ions, electronic diffusion, and the facile electrolyte infiltrations. As a result, the electronic and ionic conductivity of the self-organized TiO_2 thin film were promoted to a large extent.

2. Experimental section

2.1. Material preparation

The TiO_2 film electrode was prepared via a typical hydrothermal procedure, as we previously reported [30–32]: A piece of clean Ti substrate (with a thickness of 0.05 mm, 99.5% in purity) was transferred into a 100-mL Teflon-lined stainless steel autoclave with 10 mL of ethanol and 80 mL of 0.5 mol/L NaOH solution. The sealed autoclave was heated to 220 °C and maintained for 16 h (with a heating rate of 3 °C/min). After washing with deionized water several times, the precursor was treated with ion exchange to substitute Na^+ into H^+ in 100 mL of 0.1 M HCl for 6 h. Finally, the as-prepared hydrogen titanate was heated to 400 °C for 4 h (with a temperature ramp of 3 °C/min) to obtain the free-standing TiO_2 film.

In the following synthesis, $SnCl_4 \cdot 5H_2O$ (20 g) and 8 mL of HCl were added to 100 mL of isopropyl alcohol and stirred for 10 min to form a homogeneous solution. The solution was then coated on the as-prepared TiO_2 film electrode gently with a soft brush. After drying at 90 °C for 5 min, the hybrid film electrode was calcined in air at 500 °C for 1 h. After repeating the coating process twice more, the final electrode was obtained when the sample cooled to room temperature.

2.2. Materials characterizations

Powder X-ray diffraction patterns were tested on a Rigaku MiniFlex600 X'pert. Morphologies of the samples were examined with a HITACHI S-4800 and JEM-2100. Area's Energy Dispersive Spectra was conducted using an energy dispersive X-ray device attached to a HITACHI S-4800 SEM.

2.3. Electrochemical performance characterization

The electrochemical performances were characterized in CR2016 coin cells with Celgard 2400 (Celgard, Inc., USA) as the separator and 1 mol/L $LiPF_6$ in a 1:1:1 (V: V: V) mixture of EC, DMC and DEC as the electrolyte. Galvanostatic charge/discharge experiments were performed at different current densities between 0.01 and 3.0 V (*vs* Li/Li^+) by using the Land battery test system (LAND-V34, Land Electronic Co., Ltd., Wuhan). Cyclic voltammetry (CV) and electrochemical impedance spectroscopy (EIS) were measured with an Autolab electrochemical workstation (PGSTAT302 N, Switzerland). CV tests were conducted with a scan rate of 0.1 mV s^{-1} between 0.01 and 3.0 V (*vs* Li/Li^+). For EIS tests, the frequency range was from 10^5 to 10^{-2} Hz.

3. Results and discussion

The TiO_2@SnO_2 network film electrode was synthesized by a three-step process, as illustrated in Fig. 1. Firstly, $H_2Ti_3O_7$ nanowire film electrode was prepared by a typical hydrothermal procedure. Followed by a calcination step in air, the TiO_2 nanowire film electrode was successfully obtained. Then, SnO_2 nanoparticles were dispersed on the surface of the TiO_2 nanowires via a pyrolysis process in air.

Fig. 2 presents the X-ray diffraction patterns of TiO_2 and TiO_2@SnO_2 network film electrodes. Both TiO_2 and TiO_2@SnO_2 electrodes showed the characteristic peaks of anatase crystalline form of TiO_2 (JCPDS No. 89-4921) [33–35], which were found at $2\theta = 25.2°$, 37.8°, 48.4°, 62.8°, 76.0°, except for the sharp diffraction positions at $2\theta = 40.2°$, 53.0°, 70.6° that belonged to the metal titanium current collector (JCPDS No. 89-2762). For TiO_2@SnO_2, three small and broad peaks were located at 26.7°, 34.1° and 51.9°.

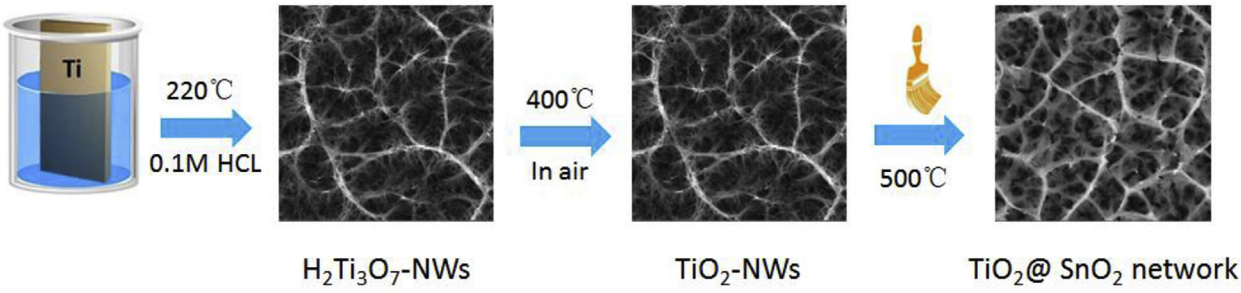

Fig. 1. Schematic illustration of the synthetic process of the TiO_2@SnO_2 network film electrode.

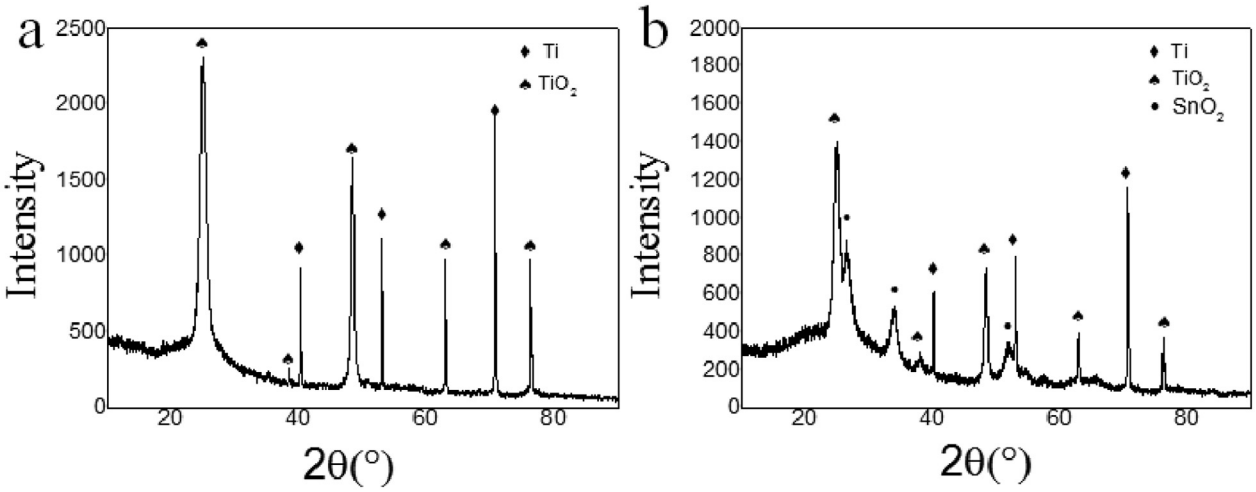

Fig. 2. XRD patterns of TiO_2 and TiO_2@SnO_2 network film electrodes.

According to the literature, such peaks are related to the nano-scale rutile-phase SnO_2 (JCPDS No. 72-1147) [36]. From these results, it was obvious that the loading of SnO_2 on the TiO_2 film electrode via the pyrolysis process would be successful and effective without any negative impact on the crystallinity of the TiO_2 during the SnO_2 loading.

Fig. 3 shows the scanning electron microscope (SEM) images of TiO_2 and TiO_2@SnO_2 electrodes. Here, all of the samples showed a 3D nano-network structure, composed of many homogeneous 1D nanowires, of which the column diameter was approximately 20–30 nm. After the SnO_2 pyrolysis reaction, it was observed that SnO_2 was successfully adhered to the surface of the TiO_2 nano-network structure (Fig. 3d ~ f). SnO_2 was deposited not only on the single TiO_2 nanowires but also on the joint of the TiO_2 nanowires. Finally, a more integrated and uniform conductive network was formed for the TiO_2@SnO_2 film electrode. The special 3D nano-network structure and the tight connection between TiO_2 and SnO_2 could be expected to provide short pathways for lithium ions, electronic diffusion and the facile electrolyte infiltration throughout the thin film electrode.

The distribution of crystalline SnO_2 nanoparticles within the TiO_2 network was further characterized by transmission electron microscopy (TEM), as show in Fig. 4. The TEM images clearly show that the size of the uniform SnO_2 nanoparticles adhered to the surface of the nanowires (Fig. 4a and b) was approximately 10–20 nm. Fig. 4b shows the high-resolution TEM image recorded from the selected area, which revealed the lattice fringes of 0.341 and 0.186 nm, corresponding to the (110) plane of rutile-phase SnO_2 and (200) plane of anatase-phase TiO_2, respectively [37,38]. Furthermore, the SAED pattern illustrated clear (101) lattice spacing of 0.349 nm and (200) lattice spacing of 0.185 nm, which were consistent with the d-spacing of an anatase-phase TiO_2 structure [32,39–41]. All of these results further confirmed that the SnO_2 loading did not have any negative impact on the crystallinity and purity of the TiO_2.

The distribution of SnO_2 nanoparticles on the TiO_2@SnO_2 composite was further confirmed by a high-angle annular dark-field scanning transmission electron microscope (HAADF-STEM) and line scan energy dispersive X-ray spectroscopy (EDX) of the arrow position shown in Fig. 5. According to the HAADF-STEM image, the uniformly distributed SnO_2 decorated on the surface of the TiO_2@SnO_2 composite was clearly distinguishable. The corresponding line-scan EDX profile further indicated that the TiO_2 nanowire width was approximately 50 nm and that there was a uniform deposition of a 10-20-nm-thick SnO_2 layer on the TiO_2 nanowire, which matched well with the above-mentioned inference.

Fig. 6 shows the galvanostatic cycling performance of the TiO_2@SnO_2 electrode at the current density of 200 mA g^{-1} between 0.01 and 3.0 V. In the first cycle, SnO_2 displayed the initial charge/discharge capacity of 691/1099 mAh g^{-1} with an enhanced coulomb efficiency of 62.9%, which was approximately 30%–40% for the SnO_2 electrode as reported in the recent literature [42–44]. The capacity loss in the first cycle may be attributed to the irreversible reaction from SnO_2 and Li to metallic Sn and Li_2O, which leads to the formation of SEI film and the $Li_xTi_{1-x}O_2$ phase by the reduction of TiO_2. However, the $Li_xTi_{1-x}O_2$ would not oxidize again during the subsequent cycles and furthermore served as a favorable

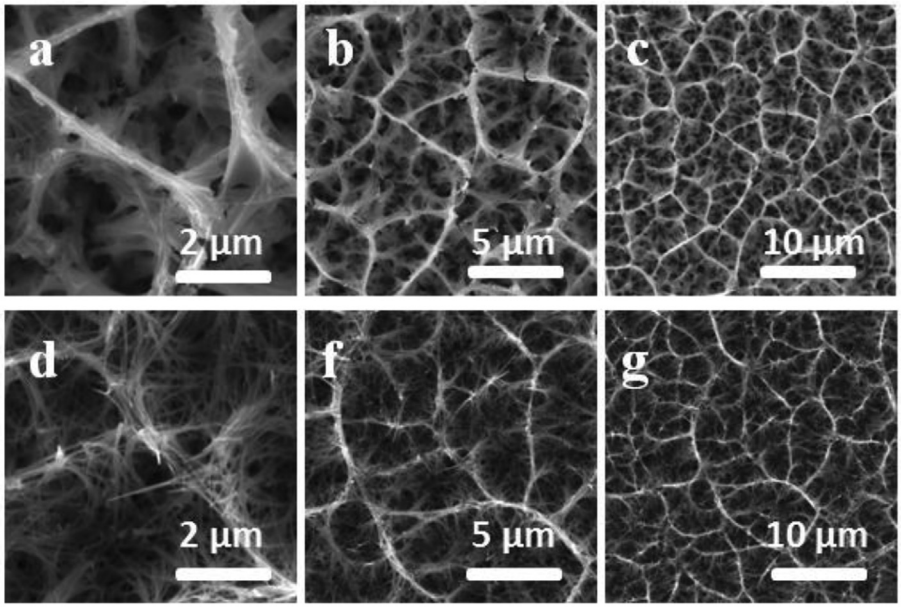

Fig. 3. SEM images of (a, b, c) TiO_2 and (d, e, f) TiO_2@SnO_2 network film electrodes.

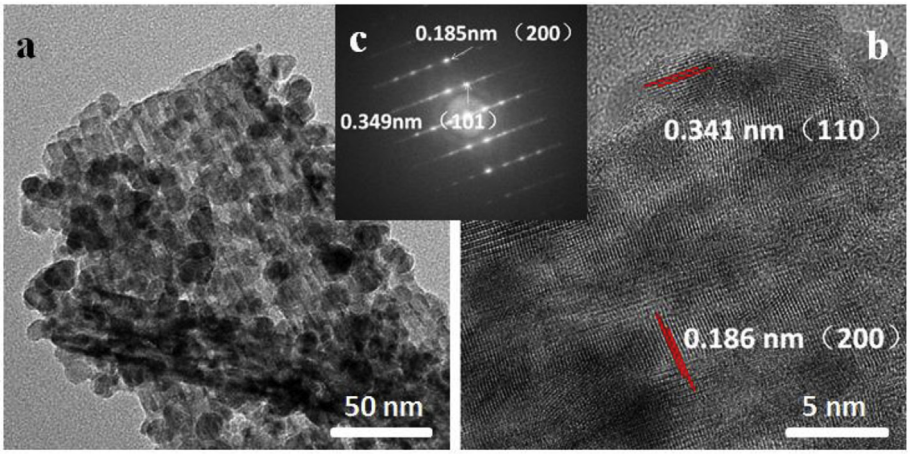

Fig. 4. (a) TEM image of TiO_2@SnO_2 composite, (b) magnified TEM image of TiO_2@SnO_2 composite, (c) the corresponding SAED pattern.

ionic and electronic conductive layer. Thus, the improved initial coulombic efficiency could be due to the TiO_2 setting a protective layer to restrict the irreversible reaction. As expected, the hybrid electrode also improved the cycle stability for SnO_2 [45–48] and delivered a reversible capacity of 834 mAh g^{-1} after 100 cycles with a capacity retention of 120%, showing outstanding performance and stability.

Along with the excellent cycling stability, the TiO_2@SnO_2 electrode also exhibited a perfect rate capability. As shown in Fig. 7, the initial reversible capacity was 939 mAh g^{-1} at the current density of 100 mA g^{-1}. After 10 cycles, the reversible capacity was maintained as 930 mAh g^{-1} with a high coulombic efficiency of 99.1%. When the current density increased from 200 to 400, 800 and 1600 mA g^{-1}, the hybrid electrode also exhibited relatively high capacity, varying from 796, 705, 564 to 464 mAh g^{-1}. When the current density was reversed back to 100 mA g^{-1}, the reversible capacity recovered a high value of 840 mAh g^{-1} with a coulombic efficiency of 98.7%. Fig. 7b shows the corresponding discharge/charge profiles. The initial plateau of SnO_2 in the potential ranged from 1.10 to 0.50 V, representing the typical conversion reaction between SnO_2 and Li^+, which resulted in the formation of Sn and Li_2O. The other region had a plateau that was observed at 1.75 V, which belonged to the classic Li^+ insertion/extraction in TiO_2 [49].

In Fig. 8, there are four main couples of oxidation-reduction peaks. The obvious couple of peaks located between 2.0 and 1.5 V was attributed to the Li^+ storage of SnO_2 and TiO_2. The cathodic/anodic broad peaks located at 1.5 and 1.7 V represented the typical Li^+ insertion/extraction process in the anatase TiO_2 [32]. The process was divided into two parts: The first part, from 3.0 to 1.75 V, was the formation of a solid solution phase, which was dependent on Li^+ insertion into the *I4 1/amd* tetragonal anatase lattice (Li_x-TiO_2) [50,51]. The second voltage region was the platform at 1.75 V, which belonged to a two-phase reaction between the Li-poor tetragonal anatase Li_xTiO_2 and orthorhombic $Li_{0.5}TiO_2$ phases [52,53]. The couple of oxidation-reduction peaks between 1.5 and 0.8 V were related to the dealloying reaction of Li_xSn and the oxidation of the metallic Sn particles. The big oxidation-reduction peaks at around 0.8 V in the initial cycle were ascribed to a two-

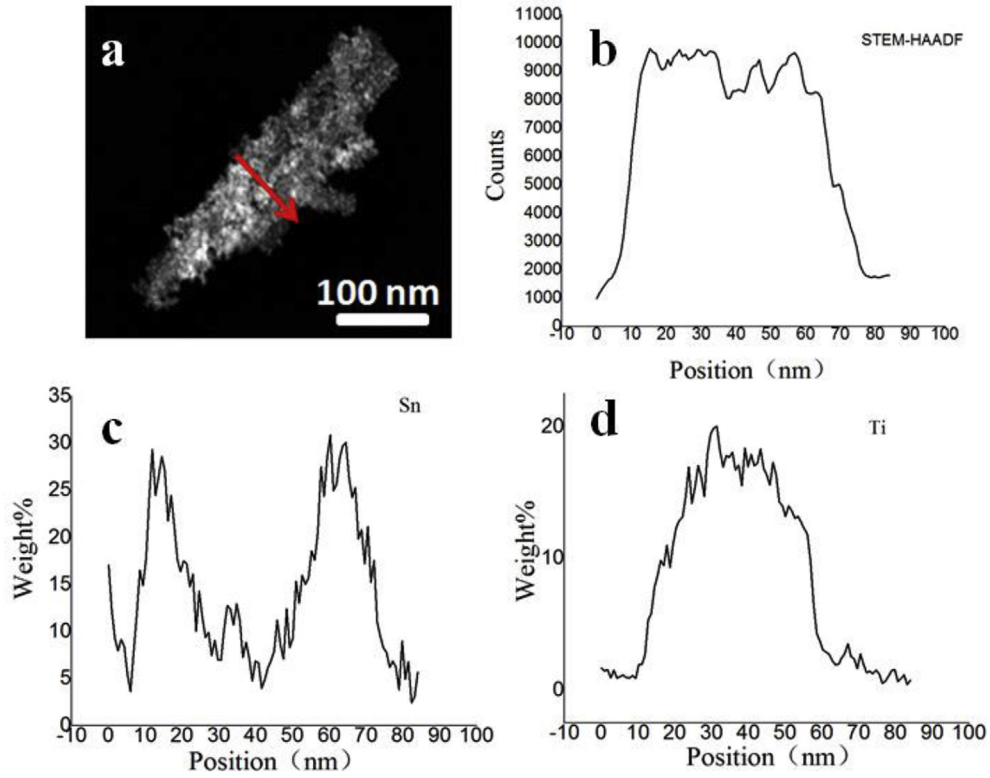

Fig. 5. (a) HAADF-STEM image and (b, c, d) the corresponding line scan EDX of the arrow position.

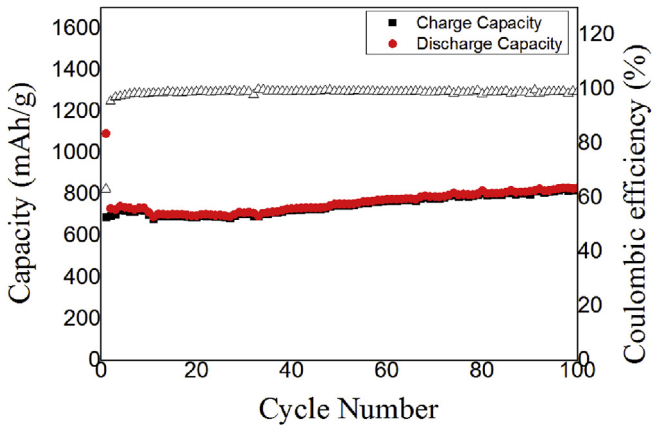

Fig. 6. Cycling performance of the TiO_2@SnO_2 electrode with a current density of 200 mA g^{-1} based on the total mass of the hybrid.

part reactions: One part was the irreversible reaction between SnO_2 and Li^+, as shown in equation (1) [54]. The other part was caused by the formation of SEI film. Since the total process loses many active Li^+, the related peaks get rapidly weaker and even disappear in the subsequent cycles. The broad oxidation-reduction peaks at around 0.05 V were attributed to the alloying between Sn and Li^+ as shown in equation (2) [54–56].

$$4Li^+ + SnO_2 + 4e^- = Sn + 2Li_2O \quad (1)$$

$$xLi^+ + Sn + xe^- = Li_xSn\ (0 \le x \le 4.4) \quad (2)$$

To further investigate the process kinetics of electrode materials, EIS tests were performed at the open circuit voltage before cycling and after the 20th cycle. As displayed in Fig. 9, before cycling, the Nyquist plots of the electrode included a semicircle in the high frequency range and a slope line in the low frequency range. For the cycled electrode, the Nyquist plots included a small semicircle in the high frequency range, a large semicircle in the middle frequency range and a slope line in the low frequency range. The equivalent circuit is shown in the inset. The concave semicircle may represent the sum of the ohmic resistance (related to the transport of lithium ions and electrons through electrolytes, porous membranes, wires, and active material particles, R_s) and the charge transfer resistance (R_{ct}). The formation of the SEI film during cycling of the electrode increased the diffusion resistance of the lithium ions through the SEI film (R_f) [57–59] and resulted in the one small extra semicircle in the high frequency range. The slope simultaneously corresponded to the Warburg impedance related to the diffusion of lithium ions into the bulk electrodes (Z_w), and the constant phase element (CPE) was used to substitute an ideal double layer capacitor.

Table 2 shows the fitting results; the small error (less than 5%) represents the accuracy of the analog circuit. It can be found that the $R_s + R_f$ value after cycling increased (15.335 Ω) somewhat compared with that before cycling (1.730 Ω), which indicated the formation of the SEI film [60,61]. In addition, the increase in R_{ct} indicated that the activity of the insertion/extraction reaction of lithium ions was reduced and that the electrochemical reaction process is more difficult, which caused the capacity of the electrode to decay [62].

In order to illuminate the superiority of the 3D network TiO_2@SnO_2 film structure, we have analyzed the post-cycling microstructure characterization by SEM. As shown in Fig. 10,

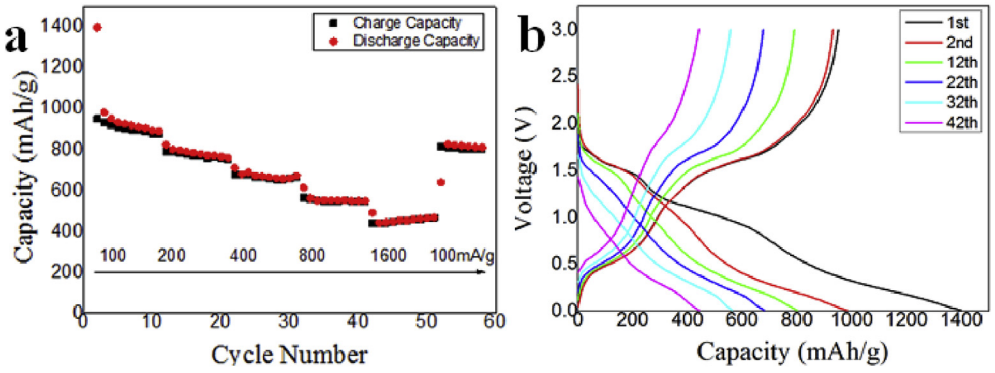

Fig. 7. (a) Charge capacities and rate capabilities of the prepared TiO_2@SnO_2 electrode at different current densities, and (b) the corresponding voltage profiles.

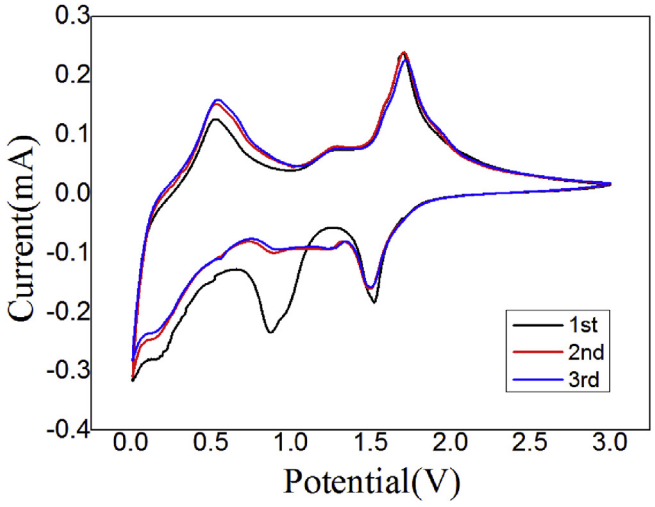

Fig. 8. Cyclic voltammetry for TiO_2@SnO_2 electrode at a scanning rate of 0.1 mV s^{-1} from 0.01 to 3.0 V.

compared with the TiO_2@SnO_2 film electrode and pure TiO_2 film electrode, after 20 cycles, the SnO_2 nanoparticles tightly adhere to the TiO_2 nanowires and the volume change is restrained to a great extent. Based on the above results, we can conclude that the 3D TiO_2 nano-network can act as a stable barrier to prevent SnO_2 nanoparticles from agglomerating and serve as a buffering space to accommodate the pulverization of SnO_2, thus resulting in the stability of the structure and electrochemical performance.

Table 2
Impedance parameters of the SnO_2 hybrid electrodes before cycling and after the 20th cycle.

Sample	$R_s + R_f$ (Ω)	Error%	R_{ct} (Ω)	Error%
Before cycling	1.730	1.031	73.300	0.556
After cycling	15.335	3.837	78.290	2.110

4. Conclusions

Assisted by the hydrothermal and pyrolysis synthesis method, we have developed an efficient approach to fabricate the TiO_2@SnO_2 film electrode with a special 3D nano-network structure. The porous netlike TiO_2@SnO_2 film electrode exhibits superior electrochemical performance with a favorable combination of long cycle life (834 mAh g^{-1} can be maintained after 100 cycles at a current density of 200 mA g^{-1}) and remarkable rate capability (796, 705, 564 and 464 mAh g^{-1} at 200, 400, 800 and 1600 mA g^{-1}, respectively). The outstanding electrochemical properties can be attributed to the special 3D nano-network structure, the well-dispersed SnO_2 nanoparticles and the compact connection between the TiO_2 and SnO_2 particles. The hybrid network could act as stable barriers to prevent SnO_2 from agglomeration and serve as a space to buffer the specific pulverization of SnO_2.

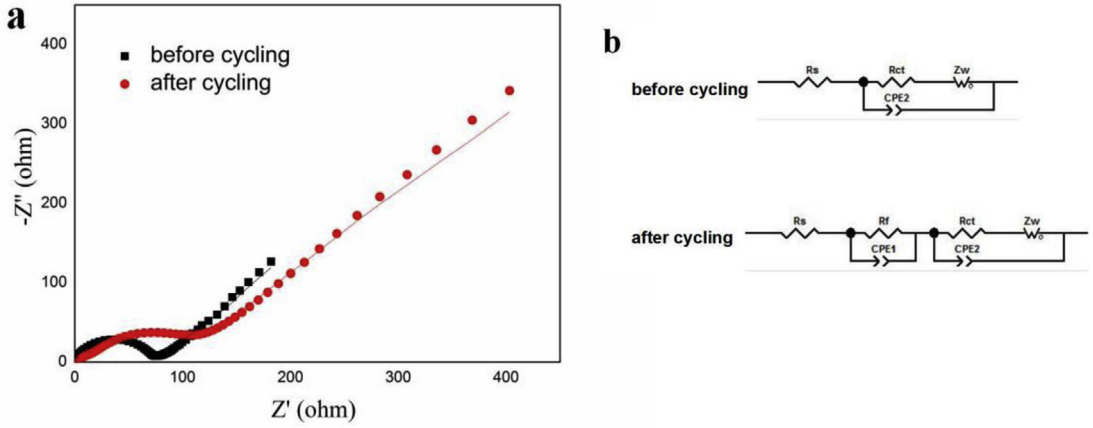

Fig. 9. (a) Electrochemical impedance spectra of the as-prepared electrodes before cycling and after the 20th cycle; (b) equivalent circuits used for fitting the experimental data.

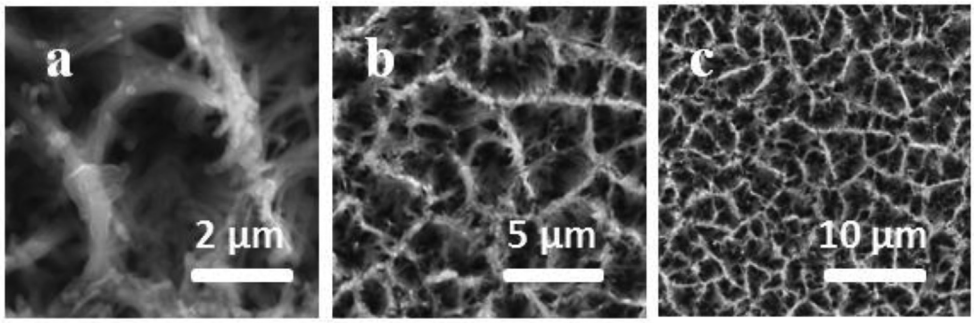

Fig. 10. SEM and magnified SEM images of TiO_2@SnO_2 film electrodes after 20 cycles at a current density of 200 mA g^{-1}.

Acknowledgements

Financial support from the National Natural Science Foundation of China (No.51604132 and 51764029) and the Provincial Natural Science Foundation of Yunnan (No.2017FB085 and 2017FD091) is gratefully acknowledged. The authors also wish to express their thanks to Dr. Nayaka Girish Praveen for his valuable suggestions on manuscript revision.

References

[1] M. Zhang, Y. Li, E. Uchaker, S. Candelaria, L. Shen, T. Wang, G. Cao, Homogenous incorporation of SnO_2 nanoparticles in carbon cryogels via the thermal decomposition of stannous sulfate and their enhanced lithium-ion intercalation properties, Nano Energy 2 (2013) 769–778.
[2] J. Zhu, G. Zhang, X. Yu, Q. Li, B. Lu, Z. Xu, Graphene double protection strategy to improve the SnO_2 electrode performance anodes for lithium-ion batteries, Nano Energy 3 (2014) 80–87.
[3] S.Y. Chang, S.F. Chen, Y.C. Huang, Synthesis, structural correlations, and photocatalytic properties of TiO_2 nanotube/SnO_2-Pd nanoparticle heterostructures, J. Phys. Chem. C 115 (2011) 1600–1607.
[4] C. Cheng, H.J. Fan, Branched nanowires: synthesis and energy applications, Nano Today 7 (2012) 327–343.
[5] G. Du, Z. Guo, P. Zhang, Y. Li, M. Chen, D. Wexler, H. Liu, SnO_2 nanocrystals on self-organized TiO_2 nanotube array as three-dimensional electrode for lithium ion microbatteries, J. Mater. Chem. 20 (2010) 5689–5694.
[6] J.H. Jeun, K.Y. Park, D.H. Kim, W.S. Kim, H.C. Kim, B.S. Lee, H. Kim, W.R. Yu, K. Kang, S.H. Hong, SnO_2@TiO_2 double-shell nanotubes for a lithium ion battery anode with excellent high rate cyclability, Nanoscale 5 (2013) 8480–8483.
[7] J.S. Chen, D. Luan, C.M. Li, F.Y.C. Boey, S. Qiao, X.W. Lou, TiO_2 and SnO_2@TiO_2 hollow spheres assembled from anatase TiO_2 nanosheets with enhanced lithium storage properties, Chem. Commun. 46 (2010) 8252–8254.
[8] X. Hou, X. Wang, B. Liu, Q. Wang, Z. Wang, D. Chen, G. Shen, SnO_2@TiO_2 heterojunction nanostructures for lithium-ion batteries and self-powered UV photodetectors with improved performances, Chem. Electro. Chem. 1 (2014) 108–115.
[9] X. Jiang, X. Yang, Y. Zhu, K. Fan, P. Zhao, C. Li, Designed synthesis of graphene-TiO_2-SnO_2 ternary nanocomposites as lithium-ion anode materials, New J. Chem. 37 (2013) 3671–3678.
[10] S. Li, M. Ling, J. Qiu, J. Han, S. Zhang, Anchoring ultra-fine TiO_2-SnO_2 solid solution particles onto graphene by one-pot ball-milling for long-life lithium-ion batteries, J. Mater. Chem. A 3 (2015) 9700–9706.
[11] S. Han, J. Jiang, Y. Huang, Y. Tang, J. Cao, D. Wu, X. Feng, Hierarchical TiO_2-SnO_2-graphene aerogels for enhanced lithium storage, Phys. Chem. Chem. Phys. 17 (2015) 1580–1584.
[12] Q. Tian, Z. Zhang, L. Yang, S.I. Hirano, Encapsulation of SnO_2 nanoparticles into hollow TiO_2 nanowires as high performance anode materials for lithium ion batteries, J. Power Sources 253 (2014) 9–16.
[13] Z. Jiao, R. Gao, H. Tao, S. Yuan, L. Xu, S. Xia, H. Zhang, Intergrown SnO_2-TiO_2@graphene ternary composite as high-performance lithium-ion battery anodes, J. Nanoparticle Res. 18 (2016) 307.
[14] H. Park, T. Song, H. Han, A. Devadoss, J. Yuh, C. Choi, U. Paika, SnO_2 encapsulated TiO_2 hollow nanofibers as anode material for lithium ion batteries, Electrochem. Commun. 22 (2012) 81–84.
[15] L. Li, B. Guan, L. Zhang, Z. Su, H. Xie, C. Wang, Controlled synthesis of mesoporous hollow SnO_2 nanococoons with enhanced lithium storage capability, J. Mater. Chem. A 3 (2015) 22021–22025.
[16] R. Demircakan, Y.S. Hu, M. Antonietti, J. Maier, M.M. Titirici, Facile one-pot synthesis of mesoporous SnO_2 microspheres via nanoparticles assembly and lithium storage properties, Chem. Mater. 20 (2008) 1227–1229.
[17] J. Lin, Z. Peng, C. Xiang, G. Ruan, Z. Yan, D. Natelson, J.M. Tour, Graphene nanoribbon and nanostructured SnO_2 composite anodes for lithium ion batteries, ACS Nano 7 (2013) 6001–6006.
[18] Y. Tang, D. Wu, S. Chen, F. Zhang, J. Jia, X. Feng, Highly reversible and ultra-fast lithium storage in mesoporous graphene-based TiO_2/SnO_2 hybrid nanosheets, Energy Environ. Sci. 6 (2013) 2447–2451.
[19] D. Wang, J. Yang, X. Li, D. Geng, R. Li, M. Cai, T.K. Sham, X. Sun, Layer by layer assembly of sandwiched graphene/SnO_2 nanorod/carbon nanostructures with ultrahigh lithium ion storage properties, Energy Environ. Sci. 6 (2013) 2900–2906.
[20] X. Li, Y. Zhang, T. Li, Q. Zhong, H. Li, J. Huang, Carbon encapsulated ultrasmall SnO_2 nanoparticles anchoring on graphene/TiO_2 nanoscrolls for lithium storage, Electrochim. Acta 147 (2014) 40–46.
[21] Q. Tian, Y. Tian, W. Zhang, J. Huang, Z. Zhang, L. Yang, Impressive lithium storage of SnO_2@TiO_2 nanospheres with a yolk-like core derived from self-assembled SnO_2 nanoparticles, J. Alloys Compd. 702 (2017) 99–105.
[22] M. Zhang, K. Yin, Z.D. Hood, Z. Bi, C.A. Bridges, S. Dai, Y.S. Meng, M.P. Paranthaman, M. Chi, In situ TEM observation of the electrochemical lithiation of N-doped anatase TiO_2 nanotubes as anodes for lithium-ion batteries, J. Mater. Chem. A 5 (2017) 20651–20657.
[23] H. Xie, M. Chen, L. Wu, Hierarchical TiO_2/SnO_2 hollow spheres coated with graphitized carbon for high-performance electrochemical Li-ion storage, Small 13 (2017), 1604283.
[24] T. Liang, R. Hu, H. Zhang, H. Zhang, H. Wang, Y. Ouyang, J. Liu, L. Yang, M. Zhu, A scalable ternary SnO_2-Co-C composite as a high initial coulombic efficiency, large capacity and long lifetime anode for lithium ion batteries, J. Mater. Chem. A (2018), https://doi.org/10.1039/c8ta00957k.
[25] Y. Wan, T. Wang, H. Lu, X. Xu, C. Zuo, Y. Wang, C. Teng, Design and synthesis of graphene/SnO_2/polyacrylamide nanocomposites as anode material for lithium-ion batteries, RSC Adv. 8 (2018) 11744–11748.
[26] X. Liu, T. Ma, L. Sun, Y. Xu, J. Zhang, N. Pinnac, Enhancing the lithium storage performance of graphene/SnO_2 nanorods by a carbon riveting strategy, ChemSusChem (2018), https://doi.org/10.1002/cssc.201702388.
[27] H. Hu, L. Wu, P. Gebhardt, X. Zhang, A. Cherevan, B. Gerke, R. Pöttgen, A. Balducci, S. Passerini, D. Eder, Growth mechanism and electrochemical properties of hierarchical hollow SnO_2 microspheres with "chest-nut" morphology, CrystEngComm 19 (2017) 6454–6463.
[28] Q. Han, F. Wang, Z. Wang, Z. Yi, Z. Na, X. Wang, L. Wang, PAN-based carbon fiber@SnO_2 for highly reversible structural lithium-ion battery anode, Ionics 24 (2017) 1049–1055.
[29] Q. Han, Z. Yi, F. Wang, Y. Wu, L. Wang, Preparation of bamboo carbon fiber and sandwich-like bamboo carbon fiber@SnO_2@carbon composites and their potential application in structural lithium-ion battery anodes, J. Alloys Compd. 709 (2017) 227–233.
[30] Y.J. Zhang, J.M. Liu, J.B. Zhao, L. Huang, X. Li, Effect of loading content of silver on lithium storage for TiO_2 net-work flexible film electrode, Chin. J. Inorg. Chem. 33 (2017) 809–816.
[31] H. Lin, X. Li, X. He, J. Zhao, Application of a novel 3D nano-network structure for Ag-modified TiO_2 film electrode with enhanced electrochemical performance, Electrochim. Acta 173 (2015) 242–251.
[32] Y. Zhang, S. Zhao, X. Zeng, J. Xiao, P. Dong, J. Zhao, S. Sun, L. Huang, X. Li, TiO_2-MoS_2 hybrid nano composites with 3D network architecture as binder-free flexible electrodes for lithium ion batteries, J. Mater. Sci. Mater. Electron. 28 (2017) 9519–9527.
[33] V. Gentili, S. Brutti, L.J. Hardwick, A.R. Armstrong, S. Panero, P.G. Bruce, Lithium insertion into anatase nanotubes, Chem. Mater. 24 (2012) 4468–4476.
[34] X. Peng, A. Chen, Large-scale synthesis and characterization of TiO_2-Based nanostructures on Ti substrates, Adv. Funct. Mater. 16 (2006) 1355–1362.
[35] X. Li, J. Zhao, S. Sun, L. Huang, Z. Qiu, P. Dong, Y. Zhang, The application of plasma treatment for Ti^{3+} modified TiO_2 nanowires film electrode with enhanced lithium-storage properties, Electrochim. Acta 211 (2016) 395–403.
[36] L. Wu, H. Yan, X. Li, X. Wang, Characterization and photocatalytic properties of SnO_2-TiO_2 nanocomposites prepared through gaseous detonation method,

Ceram. Int. 43 (2017) 1517–1521.
[37] C. Zhu, X. Xia, J. Liu, Z. Fan, D. Chao, H. Zhang, H.J. Fan, TiO_2 nanotube@SnO_2 nanoflake core-branch arrays for lithium-ion battery anode, Nano Energy 4 (2014) 105–112.
[38] S. Park, S.D. Seo, S. Lee, S.W. Seo, K.S. Park, C.W. Lee, D.W. Kim, K.S. Hong, Sb: SnO_2@TiO_2 heteroepitaxial branched nanoarchitectures for Li ion battery electrodes, J. Phys. Chem. C 116 (2012) 21717–21726.
[39] J.Y. Liao, B.X. Lei, H.Y. Chen, D.B. Kuang, C.Y. Su, Oriented hierarchical single crystalline anatase TiO_2 nanowire arrays on Ti-foil substrate for efficient flexible dye-sensitized solar cells, Energy Environ. Sci. 5 (2012) 5750–5757.
[40] B. Liu, J.E. Boercker, E.S. Aydil, Oriented single crystalline titanium dioxide nanowires, Nanotechnology 19 (2008), 505604.
[41] J.E. Boercker, E. Enache-Pommer, E.S. Aydil, Growth mechanism of titanium dioxide nanowires for dye-sensitized solar cells, Nanotechnology 19 (2008), 095604.
[42] M.S. Wang, M. Lei, Z.Q. Wang, X. Zhao, J. Xu, W. Yang, Y. Huang, X. Li, Scalable preparation of porous micron-SnO_2/C composites as high performance anode material for lithium ion battery, J. Power Sources 309 (2016) 238–244.
[43] J.Y. Huang, L. Zhong, C.M. Wang, J.P. Sullivan, W. Xu, L.Q. Zhang, S.X. Mao, N.S. Hudak, X.H. Liu, A. Subramanian, H. Fan, L. Qi, A. Kushima, J. Li, In situ observation of the electrochemical lithiation of a single SnO_2 nanowire electrode, Science 330 (2010) 1515–1520.
[44] Z. Wang, D. Luan, F.Y.C. Boey, X.W. Lou, Fast formation of SnO_2 nanoboxes with enhanced lithium storage capability, J. Am. Chem. Soc. 133 (2011) 4738–4741.
[45] M. Ebner, F. Marone, M. Stampanoni, V. Wood, Visualization and quantification of electrochemical and mechanical degradation in Li ion batteries, Science 342 (2013) 716–720.
[46] S.W. Kim, T.H. Han, J. Kim, H. Gwon, H.S. Moon, S.W. Kang, S.O. Kim, K. Kang, Fabrication and electrochemical characterization of TiO_2 three-dimensional nanonetwork based on peptide assembly, ACS Nano 3 (2009) 1085–1090.
[47] J.S. Chen, X.W. Lou, The superior lithium storage capabilities of ultra-fine rutile TiO_2 nanoparticles, J. Power Sources 195 (2010) 2905–2908.
[48] H. Zhang, W. Ren, C. Cheng, Three-dimensional SnO_2@TiO_2 double-shell nanotubes on carbon cloth as a flexible anode for lithium-ion batteries, Nanotechnology 26 (2015), 274002.
[49] Y. Wang, X. Ding, L. Huang, Y. Xu, Y. Zuo, S. Kang, L. Cui, Critical influence of carbon nitride self-assembly coating on the electrochemical performance of SnO_2-TiO_2 nanocomposite anode material for lithium ion battery, Int. J. Electrochem. Sci. 11 (2015) 2461–2472.
[50] Y. Ren, L.J. Hardwick, P.G. Bruce, Lithium intercalation into mesoporous anatase with an ordered 3D pore structure, Angew. Chem. Int. Ed. 49 (2010) 2570.
[51] J.Y. Shin, D. Samuelis, J. Maier, Sustained lithium-storage performance of hierarchical, nanoporous anatase TiO_2 at high rates: emphasis on interfacial storage phenomena, Adv. Funct. Mater. 21 (2011) 3464–3472.
[52] L. Kavan, M. Grätzel, J. Rathouský, A. Zukalb, Nanocrystalline TiO_2 (anatase) electrodes: surface morphology, adsorption, and electrochemical properties, J. Electrochem. Soc. 143 (1996) 394–400.
[53] J. Wang, J. Polleux, J. Lim, B. Dunn, Pseudocapacitive contributions to electrochemical energy storage in TiO_2 (anatase) nanoparticles, J. Phys. Chem. C 111 (2007) 14925–14931.
[54] T.D. Hatchard, J.R. Dahn, In situ XRD and electrochemical study of the reaction of lithium with amorphous silicon, J. Electrochem. Soc. 151 (2004) A838–A842.
[55] J. Wu, H. Chen, I. Byrd, S. Lovelace, C. Jin, Fabrication of SnO_2 asymmetric membranes for high performance lithium battery anode, ACS Appl. Mater. Interfaces 8 (2016) 13946–13956.
[56] N. Nitta, G. Yushin, High-capacity anode materials for lithium-ion batteries: choice of elements and structures for active particles, Part. Part. Syst. Char. 31 (2014) 317–336.
[57] D. Aurbach, M.D. Levi, E. Levi, H. Teller, B. Markovsky, G. Salitra, U. Heider, L. Heider, Common electroanalytical behavior of Li intercalation processes into graphite and transition metal oxides, J. Electrochem. Soc. 145 (1998) 3024–3034.
[58] E. Barsoukov, J.H. Kim, J.H. Kim, C.O. Yoon, H. Lee, Kinetics of lithium intercalation into carbon anodes: in situ impedance investigation of thickness and potential dependence, Solid State Ionics 116 (1999) 249–261.
[59] Q. Zhuang, S. Xu, X. Qiu, Y. Cui, L. Fang, S. Sun, Diagnosis of electrochemical impedance spectroscopy in lithium ion batteries, Prog. Chem. 6 (2010) 1044–1057.
[60] Z. Yang, Q. Meng, Z. Guo, X. Yu, T. Guo, R. Zeng, Highly uniform TiO_2/SnO_2/carbon hybrid nanofibers with greatly enhanced lithium storage performance, J. Mater. Chem. A 1 (2013) 10395–10402.
[61] S. Li, M. Ling, J. Qiu, J. Han, S. Zhang, Anchoring ultra-fine TiO_2-SnO_2 solid solution particles onto graphene by one-pot ball-milling for long-life lithium-ion batteries, J. Mater. Chem. A 3 (2015) 9700–9706.
[62] L.J. Yang, X.Q. Cheng, Y.L. Ma, S.F. Lou, Y.Z. Cui, T. Guan, G.P. Yin, Changing of SEI film and electrochemical properties about MCMB electrodes during long-term charge/discharge cycles, J. Electrochem. Soc. 11 (2013) A2093–A2099.